AN IN-VITRO STUDY OF FORCES ON THE BASILAR MEMBRANE DURING MAGNETICALLY STEERED ROBOTIC INSERTION OF LATERAL-WALL COCHLEAR-IMPLANT ELECTRODE ARRAYS

by

Cameron Murdock Hendricks

A thesis submitted to the faculty of
The University of Utah
in partial fulfillment of the requirements for the degree of

Master of Science

Department of Mechanical Engineering

The University of Utah

August 2020

The University of Utah Graduate School

STATEMENT OF THESIS APPROVAL

The thesis of **Cameron Murdock Hendricks**

has been approved by the following supervisory committee members:

Jake J. Abbott ,	Chair(s)	**5 1 2020** Date Approved
Frank M. Warren ,	Member	**5 1 2020** Date Approved
Kam K. Leang ,	Member	**5 2 2020** Date Approved

by **Bruce Gale** , Chair/Dean of

the Department/College/School of **Mechanical Engineering**

and by **David B. Kieda** , Dean of The Graduate School.

ABSTRACT

Cochlear implants are neural-prosthetic devices in which an electrode array is placed inside the scala-tympani chamber of the cochlea to directly stimulate the auditory nerve to restore hearing in those with profound hearing loss. Unfortunately, the surgical implantation of the electrode array can cause trauma to the basilar membrane, which may have a permanent effect on hearing, including a loss of residual hearing. Magnetic steering of robotically inserted electrode arrays has been proven to reduce insertion forces in in-vitro and cadaver testing, which correlates with a net reduction of forces applied by the electrode array on the scala-tympani walls during insertion. However, no prior work has evaluated forces on the basilar membrane during robotic insertions of any kind. In this thesis, forces on the basilar membrane are measured in-vitro using a custom instrumented scala-tympani phantom. Forces imparted on the phantom basilar membrane are compared between robotic insertions with and without magnetic steering. We demonstrate that magnetic steering, of sufficient magnitude, significantly reduces forces on the basilar membrane for insertion depths beyond 14.4 mm, which includes the critical region in which damage to the basilar membrane most commonly occurs. This study provides compelling evidence that magnetic steering of robotically inserted electrode arrays will provide protection to the basilar membrane, compared to robotic insertion without magnetic steering.

To my wife, Amy, who has been extremely supportive in my pursuit of education

CONTENTS

LIST OF FIGURES

ACKNOWLEDGEMENTS

I wish to express my sincere appreciation to my supervisor, Dr. Jake Abbott, who has trusted me with great responsibility on this project. His efforts to guide me have been well appreciated and well received.

I also wish to acknowledge Lisandro Leon, Matt Cavilla, and David Usevitch for the work and dedication put into the project before and during my involvement. Their work has been very vital to the project, and I would like to thank them for the continual support they have shown me.

This research is part of a larger collaboration with Dr. Robert Webster at Vanderbilt University. I would like to thank him and his team—namely Trevor Bruns, Katherine Riojas, and Dominick Ropella—for the time and effort dedicated to the project, and for the creation of the robotic insertion device and magnetic sensor used in this research.

I would also like to express my gratitude to Adam Sperry for answering a significant amount of questions on computer science/robotics topics. Without his help, this thesis and research would have been much more difficult.

I wish to express my gratitude to Anandhan Dhanasingh and his team at MED-EL in Innsbruck, Austria. Anandhan and his team have fulfilled multiple requests to create the embedded magnet implants and assist with multiple questions surrounding the implants.

This research was supported by the National Institute on Deafness and Other Communication Disorders of the National Institutes of Health under Award Number R01DC013168.

CHAPTER 1

INTRODUCTION

In this chapter, we provide an introduction to this thesis. We begin with a description of the anatomy of the ear, the basics of hearing, and the mechanism of hearing loss. We then describe cochlear implants, and the trauma associated with their surgical insertion. We review robot-assisted cochlear-implant electrode-array insertion, including with magnetic steering. We then summarize the contributions of this thesis with respect to prior work. Finally, we provide an outline of the remainder of the thesis.

1.1 The Ear and Hearing

In order for the human brain to perceive sound, there are multiple systems within the ear that must work harmoniously [6, 13, 14]. As sound waves enter the ear, they are directed through the ear canal to the ear drum. These waves cause displacement of the ear drum, which induces vibration of the ossicular chain. The ossicular chain comprises three very small bones: the malleus, the incus, and the stapes. These bones create a linkage that transfers vibrations to the oval window of the cochlea. The cochlea is a conical-shaped bone located in the inner ear that acts as a structure for small organs and membranes that contribute to hearing. The cochlea contains three channels: the scala tympani, the scala media, and the scala vestibuli (Figure 1.1). These channels are coiled around an axis called the modiolus. The oval window and round window are two small membranes of the cochlea that allow displacement of fluid within the cochlea. The oval window is located at the base of the scala vestibuli, and the round window is located at the base of the scala tympani. The respective channels are connected at their apexes to allow fluid flow, which causes the two membranes to move out of phase from one another. The Organ of Corti, located in the scala media, contains small hair-like structures called stereocilia, which transduce mechanical displacement in the basilar membrane into electrical signals, which are sent to the brain via the auditory nerve.

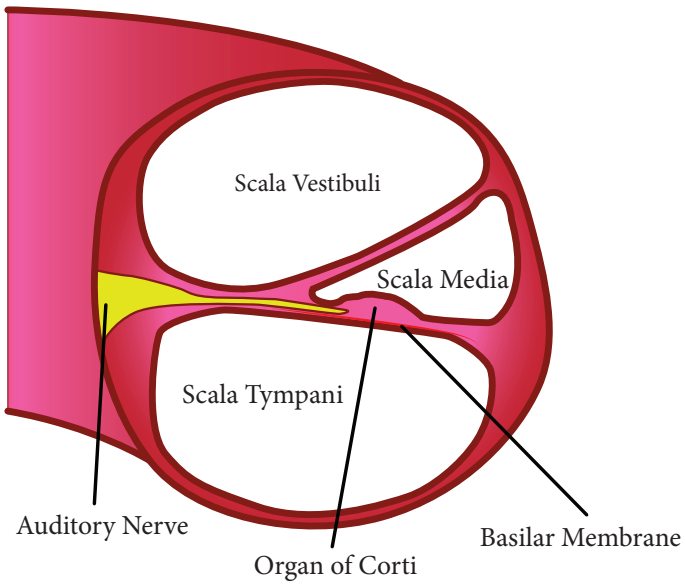

Figure 1.1: Cross section of the cochlea. Image is based on a National Institutes of Health public-domain image.

The basilar membrane is a thin membrane located between the scala media and the scala tympani. Stereocilia are spread along the length of the basilar membrane, on the scala-media side. The base of the basilar membrane is responsible for high frequencies, the apex is responsible for low frequencies, and the stereocilia between the base and the apex create a continuum in frequency sensing. The membrane is wider and more flexible at its apex, and narrower and stiffer at its base. This shape and differential stiffness causes each portion of the basilar membrane to have a different resonant frequency. As sound waves induce vibration on the oval window, the perilymph inside the scala tympani is excited and causes mechanical displacement of the basilar membrane about some point along its length. This point is determined by the input frequency. Perilymph, which resides in the scala tympani and scala vestibuli, contains sodium ions, causing it to have a net positive charge. Endolymph, which resides in the scala media, is a fluid containing a high concentration of potassium ions, causing it to have a net negative charge. This creates an electrical potential between the channels. When the stereocilia corresponding to a particular frequency become excited, ion channels open between the scala tympani and scala media, allowing the fluids to mix, which causes a drop in the electrical potential and results in the stimulation of the auditory nerve via the stereocilia. Over time, the stereocilia

can be destroyed by loud noises, toxins, or congenital diseases, leading to a loss of hearing at those specific frequencies.

1.2 Cochlear Implants

Cochlear implants are neural-prosthetic devices (Figure 1.2) in which an electrode array is placed inside the scala tympani (Figure 1.1) to provide electro-stimulation to the auditory nerve, enabling an otherwise deaf individual to hear. Cochlear implants are a two part internal/external system. The external system comprises a microphone and a digital signal processor that captures auditory signals and converts them to electrical impulses, which are then transferred to the internal system. The internal system comprises an electrode array that is placed in the scala tympani surgically. In cochlear-implant surgery, after first gaining access to the cochlea by removing some portion of the temporal bone, the surgeon will perform a cochleostomy (i.e., drill a hole in the cochlea) or puncture the round window, either of which offers a channel to insert the electrode array into the scala tympani. The electrode array has multiple electrodes along its length. When signals are received from the external unit, the internal unit directs them, depending on their frequency, to the correct electrode within the electrode array. This system is beneficial for the deaf who are born without stereocilia, those born with malformation of the cochlea, as well as older people who have lost much of their high-frequency hearing.

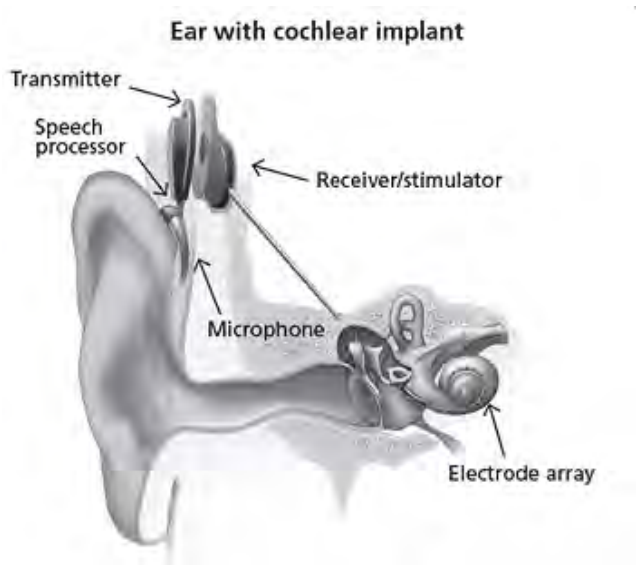

Figure 1.2: Ear with cochlear implant. National Institutes of Health public domain image.

Electrode arrays are available in multiple designs. The most common design to cause intracochlear trauma is the lateral-wall array [5, 16]. These arrays are naturally straight but flexible. As the array is inserted into the cochlea, it will use the lateral wall of the cochlea to guide it into place, and it will rest against the lateral wall after the insertion is complete. Another type of array that is common is a perimodiolar array. These arrays are naturally curved to match the geometry of the cochlea, in order to rest against the modiolus after the insertion is complete. Perimodiolar arrays must be inserted with the help of a stylet that straightens the array for the initial portion of the insertion. During insertion, the tip of the stylet is placed into the cochlea via the cochleostomy opening. As the array is advanced off the stylet it returns to its curved geometry. These arrays have been shown to cause significantly less trauma to the lateral walls and cause the array to reside closer to the modiolar axis than lateral-wall arrays [16].

This thesis considers improved insertion of lateral-wall arrays. The insertion of lateral-wall arrays can produce various forms of trauma due to scraping, folding, or buckling. If forces due to these problems are directed superiorly, trauma will be induced upon the basilar membrane (Figures 1.3 and 1.4). Studies have shown that damage can be caused due to adverse movement of either the tip or the proximal end of the electrode array [7, 8, 18, 20]. Perforation to the basilar membrane can cause the endolymph and the perilymph within the scala media and scala tympani, respectively, to mix; if this occurs, any residual hearing of the patient will be lost[19]. The risk of this adverse event is so high—both Ketten

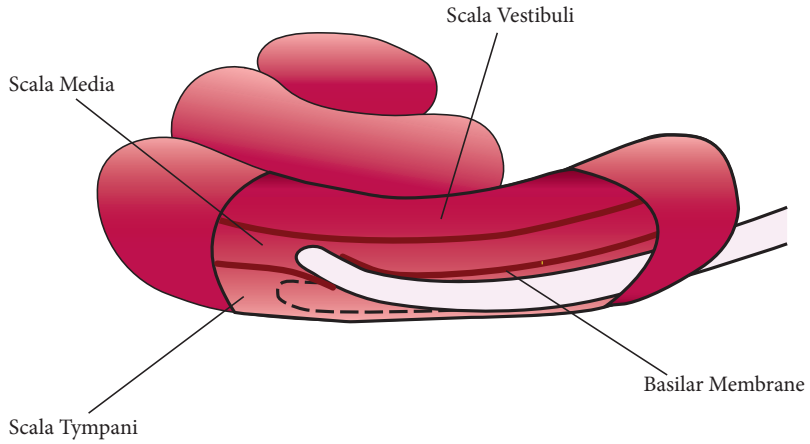

Figure 1.3: Depiction of a rupture of the basilar membrane by the electrode array. The dashed line shows the intended path in the scala tympani.

Figure 1.4: Wardrop et al. [20] reported that the most typical injury found with the Nucleus banded lateral-wall electrode array (as well as with the Nucleus Contour perimodular electrode array) was "interscalar excursion." In the case illustrated here, a lateral-wall array pierced the basilar membrane as it rounded the first turn of the cochlea near 180°. The array's tip actually bends back upon itself in the scala vestibuli and finally rests in the upper portion of the scala vestibuli with its tip facing the round window. Reprinted from Hearing Research, 203, Peter Wardrop, David Whinney, Stephen J. Rebscher, J. Thomas Roland, William Luxford, Patricia A. Leake, A temporal bone study of insertion trauma and intracochlear position of cochlear implant electrodes. I: Comparison of Nucleus banded and Nucleus Contour ™ electrodes, 14, Copyright 2005, with permission from Elsevier.

et al. [7] and Wardrop et al. [20] report that the likelihood of such an event is 25% using lateral-wall arrays.

1.3 Robotic Insertion of Cochlear-implant Electrode Arrays

A number of studies have considered the value of robotic insertion of electrode arrays. Schurzig et al. [17] compared robotic insertion of lateral-wall arrays to robotic insertion of perimodiolar arrays (using the advance-off-stylet method discussed earlier). They found that insertion forces with the perimodiolar array were significantly lower than with the lateral-wall array. Majdani et al. [12] found that when robot and surgeon used the same advance-off-stylet method with perimodiolar arrays, insertion was more reliable using the robot, whereas manual insertion-force data contained more intermittent force peaks. To the best of our knowledge, no study exists that compares robotic insertion of lateral-wall

arrays to manual insertion of lateral-wall arrays.

Multiple studies have been conducted exploring robotic insertion of steerable arrays, with different methods of steering [10, 22–24]. Zhang et al. found a 70% reduction in the insertion forces using robotic insertion combined with a tendon-based mechanically actuated steerable array [23, 24]. Zhang et al. also developed a model for the mechanical friction occurring between the array and the scala-tympani channel, which was meant devise optimal parameters for robotic insertion [22]. Leon et al. quantified insertion forces in vitro using multiple lateral-wall array types, with and without steering, using magnetic guidance as the method of steering [10]. This was accomplished by adding a small magnet to the tip of the array. The magnet at the tip of the array was actuated by a much larger external magnetic dipole source, designed to reside adjacent to the patient's head. Leon et al. specifically used a permanent magnet as the magnetic dipole source, which could be translated using a linear robotic stage and rotated using a motor. The external permanent magnet was used to generate a torque on the smaller magnet. This torque steered the implant into place and reduced insertion forces by keeping the tip of the array off of the lateral walls. The methods developed by Leon et al. are employed in this thesis.

The studies discussed above have shown that robotic insertion with steering reduces insertion forces compared to robotic insertion with no steering. However, they do not consider which specific structures of the cochlea are protected, nor which parts might be placed at additional risk. From first principles, a reduction of insertion force must correspond to a net reduction in the forces applied by the array against the walls of the cochlea. However, we are not aware of any studies that have considered the impact of robotic insertion, with or without steering, on the forces applied directly on the basilar membrane, which is arguably the most critical structure that can be damaged during the surgical insertion of the array.

1.4 Contributions of this Thesis

This thesis makes two contributions relative to the existing literature. The first is a custom scala-tympani phantom with a force-sensitive basilar membrane, for experiments characterizing insertion of cochlear-implant electrode arrays. This setup enables basilar-membrane forces, as well as insertion forces, to be measured, which has not been possible

previously.

In the second contribution of this thesis, forces imparted on the phantom basilar membrane are compared between robotic insertions of lateral-wall electrode arrays, with and without magnetic steering. We demonstrate that magnetic steering significantly reduces forces on the basilar membrane for insertion depths beyond 14.4 mm. This represents the first evidence that the addition of magnetic steering to robotically inserted arrays will help protect the basilar membrane, which is critical to maintaining residual hearing.

1.5 Organization of this Thesis

The organization of this Thesis is as follows: Chapter 2 discusses the experimental methodology, including the experimental apparatus, the statistical design, and procedure. Chapter 3 discusses results of the experiments. Chapter 4 provides further discussion of the methods and results, and suggests possible improvements to the system and methodology. Finally, Chapter 5 summarizes all that was accomplished.

CHAPTER 2

METHODS

In this chapter, we describe the experimental methodology used in this thesis. We begin with a description of the experimental apparatus, which includes a phantom cochlea with a force-sensitive basilar membrane (which is a principal contribution of this thesis), the system for robotic insertion with magnetic steering, magnetically tipped electrode arrays, and a coordinated robotic and magnetic motion planner. We then describe the statistical design of our experiment, followed by the procedure used in the experiment.

2.1 Apparatus

2.1.1 Phantom Cochlea with Force-sensitive Basilar Membrane

In order to assess forces on the basilar membrane, an open-channel scala-tympani phantom was designed and fabricated. The scala-tympani model was based on the cochleostomy model of Leon et al. [9], which is shown in Figure 2.1. The scala-tympani channel of that model was first arranged so that the modiolus was vertical (Figure 2.2(a)). Then, the channel, which has an ascending-spiral geometry, was projected onto a horizontal plane (Figure 2.2(b)). In order to create such a channel, two compromises were made. First, the ascending-spiral geometry was reduced to a planar spiral. Second, the phantom had to be reduced to just 413°, to avoid the channel from intersecting with itself. However, it is these compromises that enabled us to implement the force-sensitive basilar membrane. Next, the top of the model was removed, creating an open scala-tympani channel (Figure 2.2 (c)). This phantom, depicted in Figure 2.3, was fabricated using high-resolution stereolithography by Realize Inc. (Noblesville, IN), and it was fabricated as transparent for easy visualizations.

The top of the phantom was covered by a force-sensitive ceiling, which serves as the phantom basilar membrane. This membrane is contacted when the array deviates upward from the channel. The phantom basilar-membrane is comprised of two parts: a thin plastic

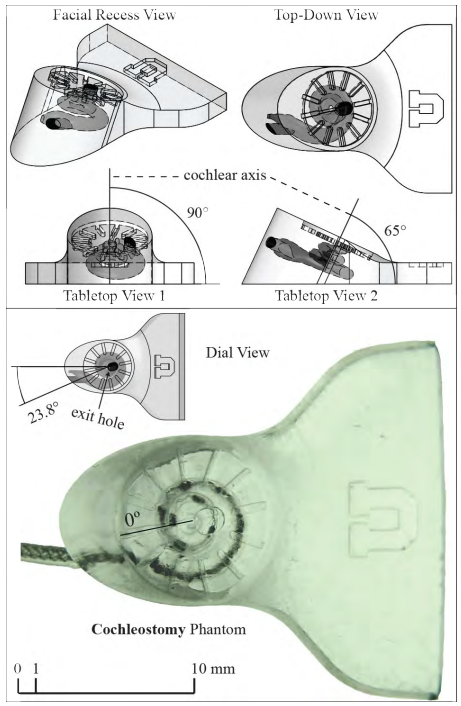

Figure 2.1: Model of scala-tympani channel. Republished with permission of American Society of Mechanical Engineers, from Scala-Tympani Phantom With Cochleostomy and Round-Window Openings for Cochlear-Implant Insertion Experiments, Leon et al., Vol. 8, 2014; permission conveyed through Copyright Clearance Center, Inc.

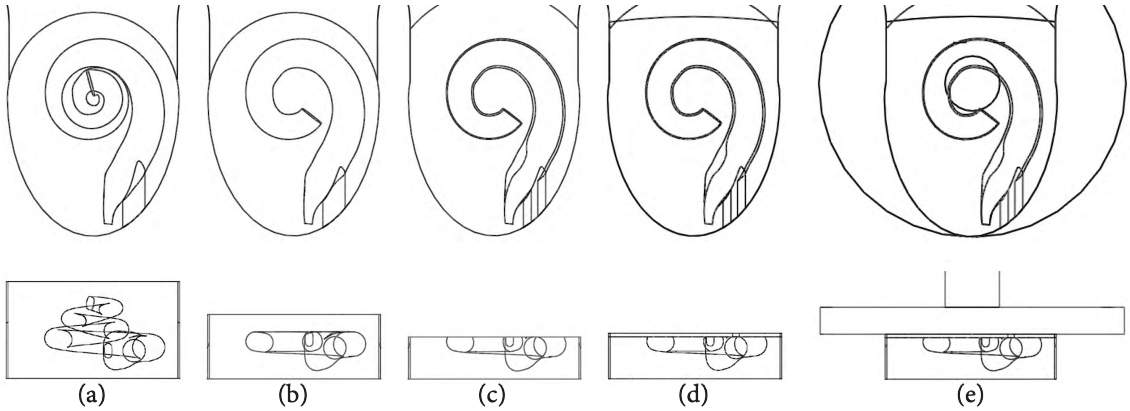

Figure 2.2: Creation of scala-tympani phantom with force-sensitive basilar membrane. Top-down views are shown on the upper row, and front views are shown on the lower row. (a) Full scala-tympani channel from the cochleostomy model of Leon et al. [9], with modiolus oriented vertically. (b) Scala-tympani channel projected onto a horizontal plane, with angular reduction. (c) Top of model removed to open the channel. (d) Thin plastic membrane attached to the top of model, with membrane enlarged for clarity. (e) Force-plate sensor placed above plastic membrane.

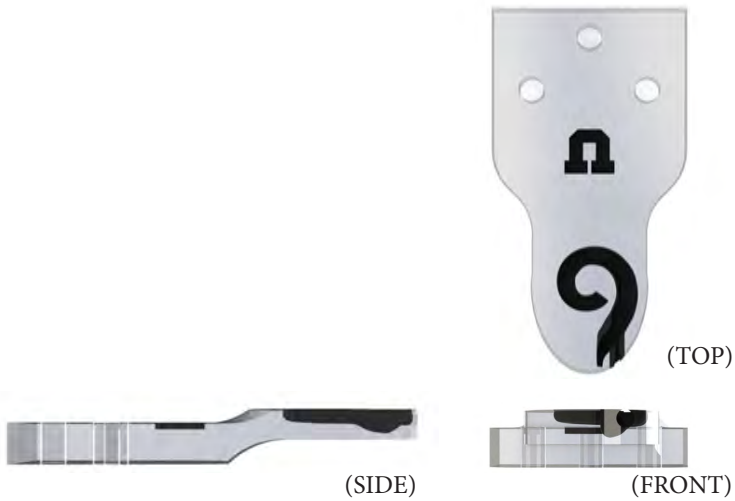

Figure 2.3: Renderings of the open-channel scala-tympani phantom, which was fabricated using stereolithography.

membrane that directly covers the channel (Figure 2.2 (d)), and a high-resolution force sensor that floats just above that membrane (Figure 2.2 (e)). The thin plastic membrane that is placed directly over the channel is made of low-density polyethylene, with a thickness of 10 μm. Its purpose is to help trap the artificial perilymph that fills the channel, and to eliminate any surface tension between the artificial perilymph and the force sensor. In pilot studies, before the inclusion of this membrane, the surface tension of the fluid caused the sensor to drift and provided unreliable force data. The force sensor used is a custom calibrated capacitance-based sensor fabricated by Nanodyne Measurement Systems (Minneapolis, MN). The sensing surface is a flat circular plate of diameter 18 mm. The sensor is designed to measure force in one degree of freedom, normal to the surface of this plate. The measured forces represent the integration of all basilar-membrane forces distributed along the length of the inserted electrode array. The sensor measures up to 147 mN with a resolution of 2.245 μN. We expected that this resolution would be sufficient to detect small changes in forces that are induced upward onto the basilar membrane. We found that the measurements in the intended direction (i.e., normal to the flat plate, which is vertical in our arrangement) are quite sensitive to forces in the unmeasured orthogonal (i.e., lateral) directions. The inclusion of the thin plastic membrane helped to mitigate lateral forces on the sensor. A rendering of the force sensor placed relative to the scala-tympani phantom is shown in Figure 2.4.

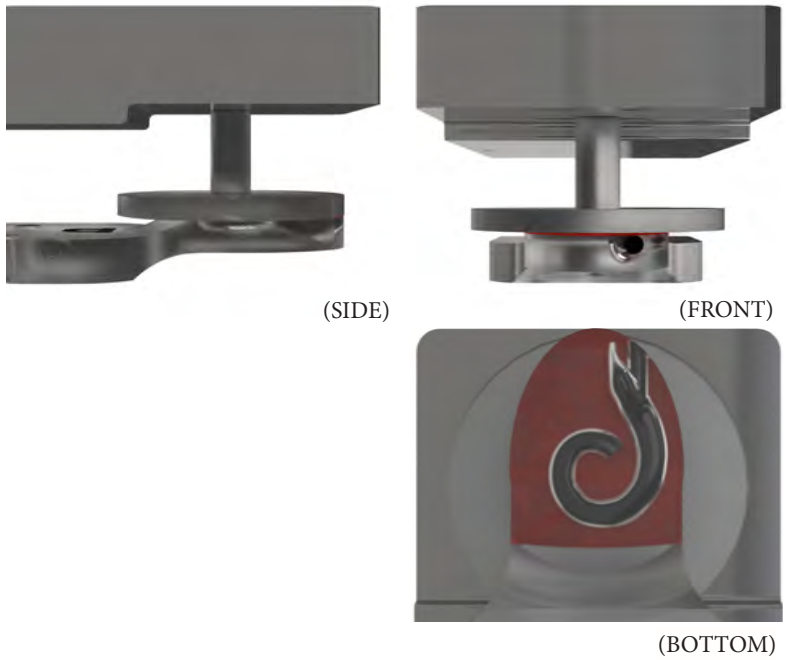

Figure 2.4: Renderings of force sensor placed above the scala-tympani phantom. For clarity, the scala-tympani channel is shown as black, and the thin plastic membrane is shown as red.

Due to the inclusion of the plastic membrane over the channel, we cannot confirm that the values measured by the force sensor are correct. In fact, we assume from first principles that the force sensor will underestimate the applied force of the electrode array, since the plastic membrane will counteract some portion of the applied force. However, in this study, we are not particularly interested in measuring the absolute value of the forces imparted on the basilar membrane. Rather, we are interested in the relative difference in forces between steered and nonsteered insertions. We will show that our setup is sufficient to distinguish these differences.

During preliminary testing, it was discovered that alignment of the planar upper surface of the scala-tympani phantom with the planar force plate would require high precision in order to record reliable data. As a result, a custom robotic alignment system was designed (Figure 2.5), which enables the scala-tympani phantom to be moved up into position beneath the stationary force sensor. The robotic alignment system comprises three linkages in a parallel (i.e., closed-chain) kinematic arrangement, with a triangular end-effector on which the scala-tympani phantom is mounted. Each linkage comprises a one-degree-of-freedom robotic linear stage (Thor Labs, Model MTS50-Z8) arranged ver-

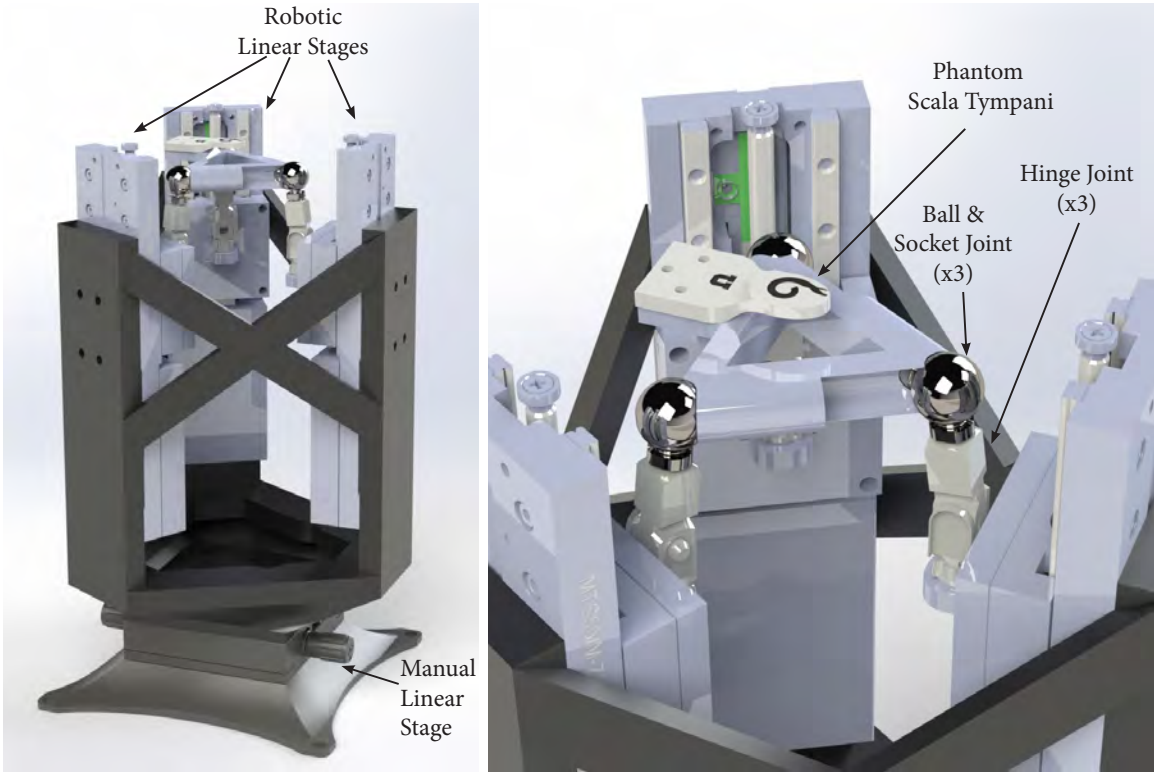

(a) Overall System (b) Zoomed View

Figure 2.5: Robotic system for precision alignment of the scala-tympani phantom.

tically, followed distally by a one-degree-of-freedom revolute (i.e., hinge) joint, followed distally by a three-degrees-of-freedom spherical (i.e., ball-and-socket) joint. Both of the passive joints have high friction, which mitigates backlash. This robotic system enables independent control over the vertical height of the end-effector and the pointing direction of its surface normal. The entire parallel robot is mounted on a one-degree-of-freedom manual linear stage (Newport, Model M-TSX-1D) arranged horizontally; this stage enables the phantom to be translated in a forward/backward direction relative to the force sensor (i.e., left/right in the SIDE view of Figure 2.4, and into/out of the image in the FRONT view). There is no need for translation in the orthogonal horizontal (i.e., lateral) direction, due to availability of alignment holes on the mechanical breadboard on which our entire experimental setup is constructed.

Alignment of the scala-tympani phantom was performed as follows. The phantom was raised up to the force plate such that the two surfaces were approximately parallel and nearly touching. Then the phantom was raised using one of the three stages until a

force was read by the force sensor, at which point the stage was backed off (i.e., lowered) until only a slight force was detected. This process was repeated for each of the three stages sequentially until advancing any of the stages farther would cause an increase in force, at which point the sensor was zeroed. The final result is a phantom that is preloaded slightly ($\leq$ 3 mN) with the sensor and no drift detected. Note that, with the given preload and zeroing of the sensor, it is possible for the force measurements to take on negative values in certain cases. This would be caused by the EA pushing downward on the scale-tympani phantom, resulting in a reduction in the preload between the scala-typani phantom and the force plate due to a small amount of compliance in the alignment system. Because our study is focused on basilar-membrane forces and not scala-typani forces, and since there is no physical mechanism for the EA to apply tension forces on the basilar membrane, any negative force readings were changed to zero.

During preliminary testing, it was found that bubbles in the channel would affect the path of the electrode array, forcing it into the scala-tympani walls. To mitigate this phenomenon, we drilled a small hole at the end of the scala-tympani channel and attached a tube to this small hole (Figure 2.6). The other end of the tube was connected to a syringe filled with the artificial perilymph. This system was used to add fluid to the channel between tests. This modification successfully removed any bubbles existing in the channel.

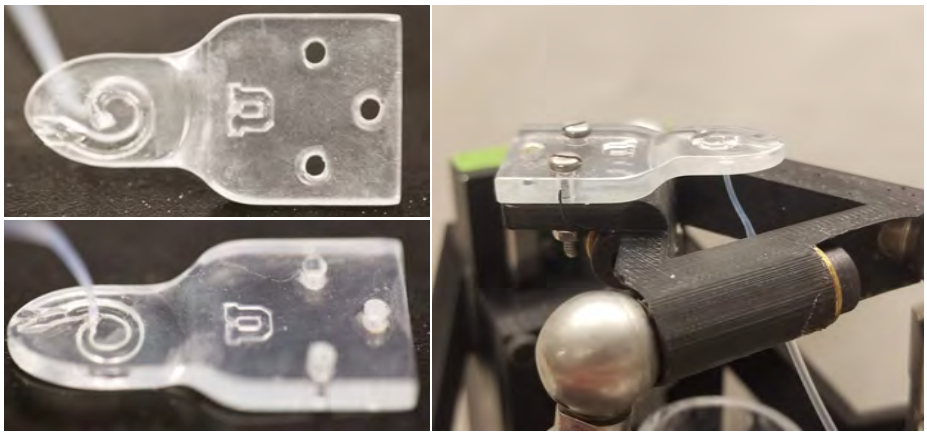

Figure 2.6: Scala-tympani phantom with fluid channel. (Top Left) Top-down view of the scala-tympani phantom, with the tube exiting from beneath.(Bottom Left) Bottom-up view of the phantom, with the tube exiting from above. (Right) Phantom mounted on the end-effector of the robotic alignment system.

2.1.2 System for Robotic Insertion with Magnetic Steering

The system that we use for magnetically steered robotic insertion of electrode arrays is a copy of the system recently described by Bruns et al. [1]. The system comprises two principal components: a robotic insertion device, and an Omnimagnet electromagnetic field source. Renderings of the complete system, integrated with the force-sensitive phantom cochlea described in Section 2.1.1, are shown in Figure 2.7, and photos are shown in Figure 2.8.

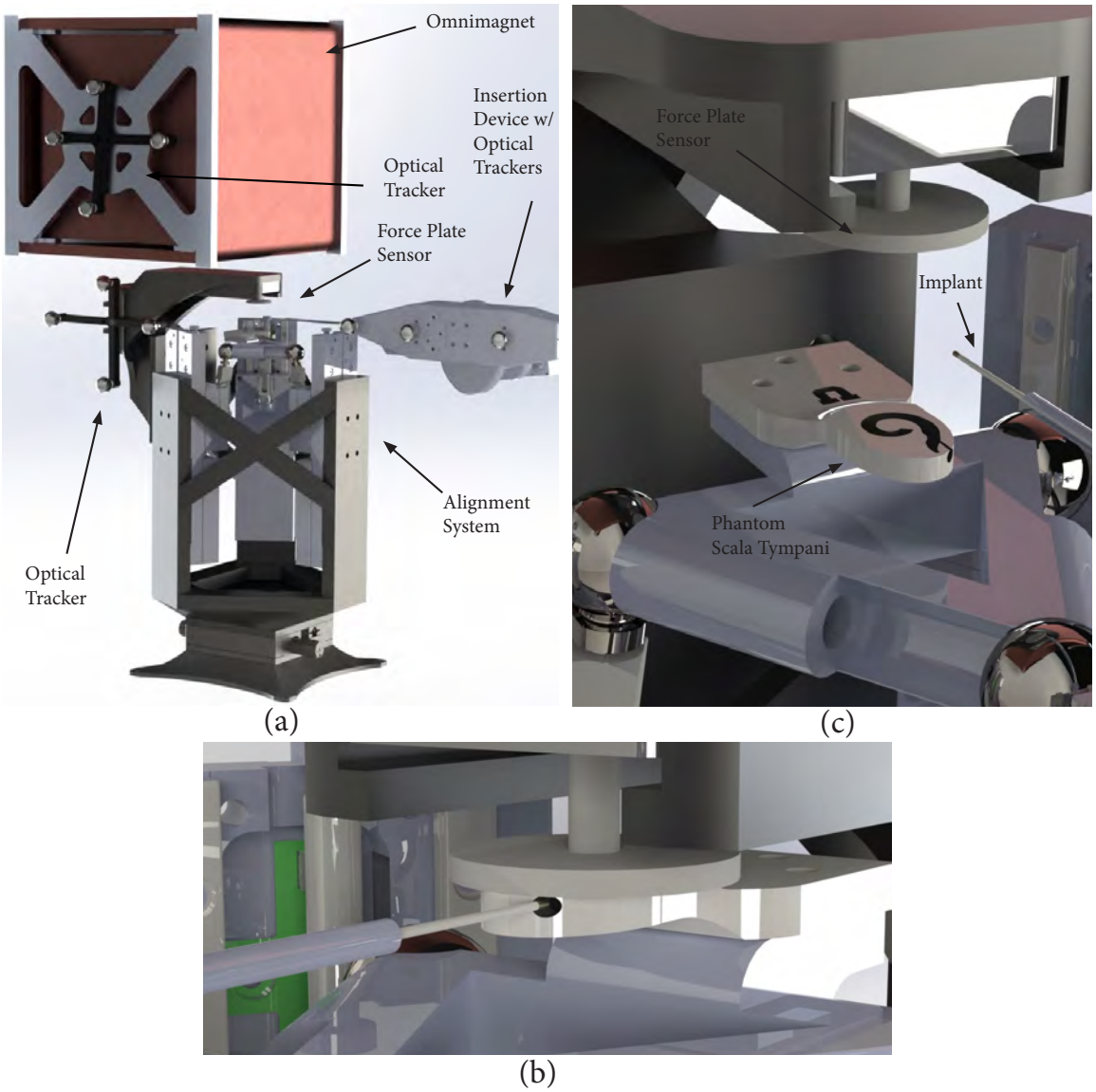

Figure 2.7: Rendering of complete experimental system. (a) Over-all system. (b) Close-up view of the electrode array being inserted into phantom. (c) Zoomed view with phantom separated from force plate.

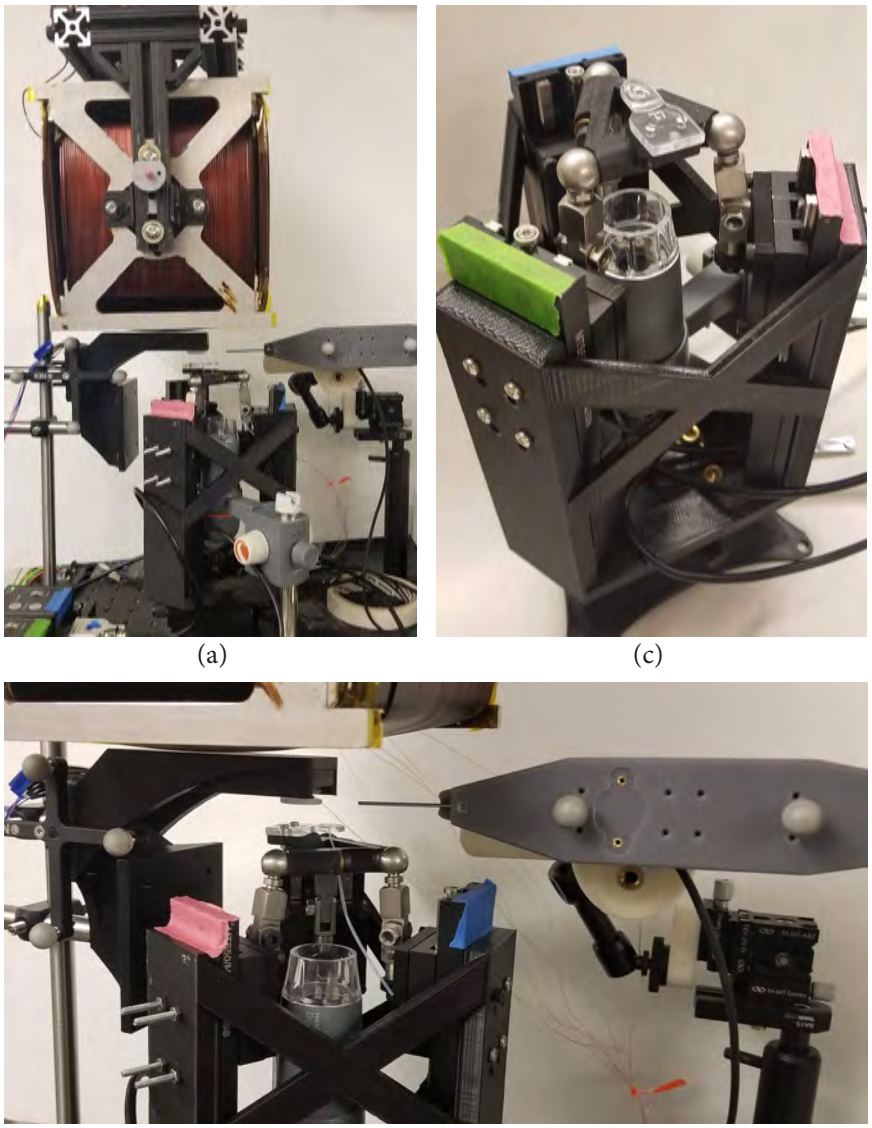

(a) (c)

(b)

Figure 2.8: Photos of complete experimental system. (a) Over-all system. (b) Close-up view of the system. (c) Alignment system. In all photos, the microscope that enables bottom-up views of the insertions can be seen.

The robotic insertion device, which was fabricated by members of Dr. Robert Webster's group at Vanderbilt University, comprises a nonmagnetic MCS Linear Stage (model SLC-1500) with a travel distance of 46 mm and subnanometer resolution to perform the insertion, which is mounted on a IMORDEN 7-inch articulating arm for coarse positioning, which is in turn mounted on a three-degrees-of-freedom linear stage (Newport M-MT-XYZ) for fine adjustment along the three principle axes.

The magnetic field is generated by an Omnimagnet [15]. An Omnimagnet comprises

three nested orthogonal electromagnets that are modeled as being colocated at the center of the device, which enables it to generate a dipole-like magnetic field with a controllable direction and magnitude (Figure 2.9). The inner, middle, and outer coils have resistances of 3.8 Ω, 4.1 Ω, and 4.4 Ω, respectively. The currents through the coils are controlled using three Advanced Motion Controls pulse-width-modulation amplifiers (Model 100A40), which are each capable of providing a continuous current of up to 50 A. The three amplifiers are powered by a single Advanced Motion Controls power supply (Model PS50A-LV), with a maximum peak current of 50 A, a maximum continuous current of 30 A, and a maximum power of 8.5 kW.

All subsystems are integrated and controlled using software written in C++, with a sampling rate of 1000 Hz. The software controls the insertion velocity (1.3 mm/s) and

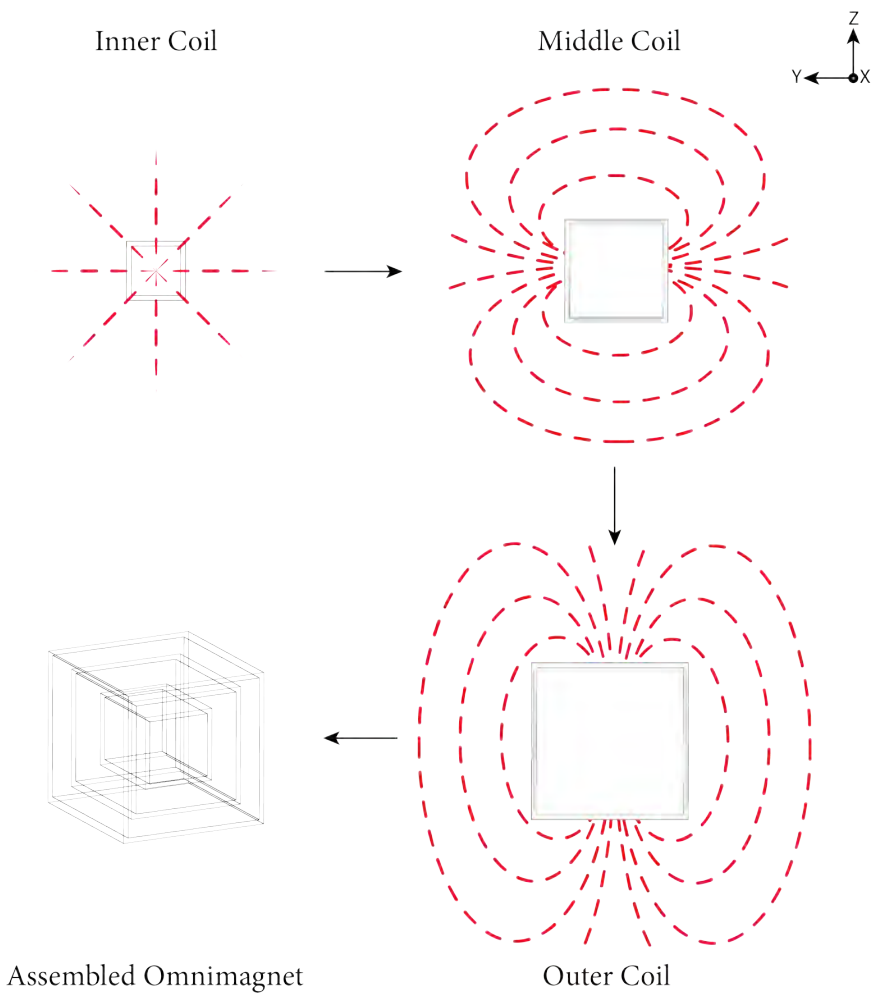

Figure 2.9: The Omnimagnet magnetic-field source.

depth of the electrode array, as well as the current commands to the three amplifiers. It also performs the magnetic-field computations required to calculate the current commands, using a method detailed in Section 2.1.4. Finally, it logs the forces applied to the plate sensor.

The center of the Omnimagnet was placed along the unit vector $\hat{p} = [0.98\ 0.21\ -0.05]^{\mathrm{T}}$, measured with respect to the center of the cochlea, which represents the optimal direction of the external magnetic source with respect to the cochlea defined in [11]. In order reduce power requirements, the Omnimagnet needs to be as close to the cochlea as possible. The final position of the Omnimagnet for all insertions is this study is $\vec{p} = [117\ 25\ -6]^{\mathrm{T}}$ mm, measured with respect to the center of the cochlea.

This Omnimagnet position is closer than the distance that will be required in a clinical system. This compromise was due to limitations of the system's magnetic field. The result of being too close is that magnetic force, which tends to pull the magnetic tip of the electrode array upward into the phantom basilar membrane—as opposed to the magnetic torque that is being used for steering—is larger than what it would be in a clinical system. Consequently, the results of our study will be conservative, since we are interested in reducing forces on the basilar membrane using magnetic steering.

A Polaris Spectra optical tracking system was used to place the Omnimagnet and insertion device relative to the phantom cochlea. The optical-tracking markers can be seen in Figure 2.7. All positioning was done to a accuracy of ± 1.5 mm and $\pm 3\,^{\circ}$.

2.1.3 Magnetically Tipped Cochlear-implant Electrode Arrays

To enable magnetic steering, two different magnetically tipped electrode arrays were fabricated by modifying MED-EL Standard (31.5 mm) arrays (Figure 2.10). The array with the smaller magnetic dipole contained two axially magnetized cylindrical permanent magnets that were connected axially and embedded in silicone at the tip of the array. Each of the individual magnets was grade N 52 NdFeB with a diameter of 0.3 mm and a length of 0.5 mm. This gave the tip of the array a dipole moment of $3.33 \times 10^{-4}\ \mathrm{A \cdot m^2}$. The array with the larger magnetic dipole was fabricated by attaching a single axially magnetized cylindrical permanent magnet to the tip of the array via an anchor (Figure 2.11). The magnet was grade N 52 NdFeB with a diameter of 0.5 mm and a length of 1 mm.

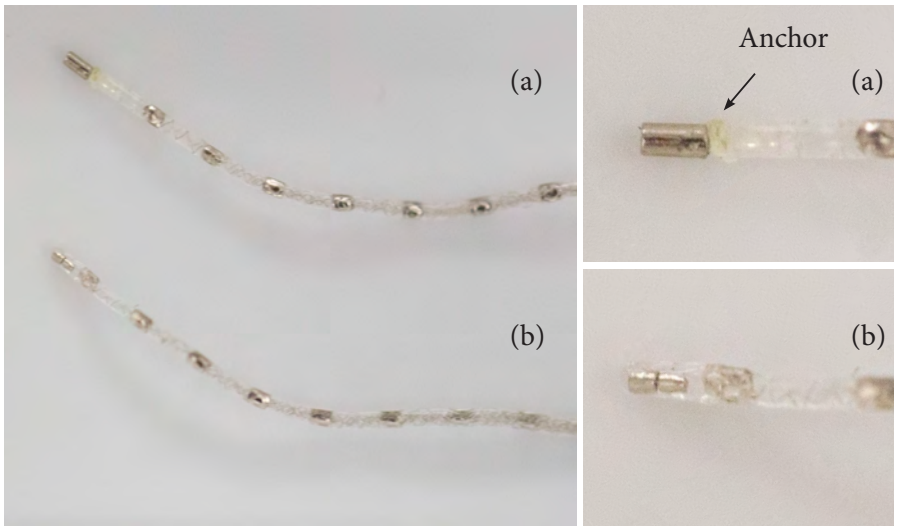

Figure 2.10: Magnetically tipped electrode arrays used in experiments. (a) Large magnet attached to tip. (b) Small magnets embedded in tip.

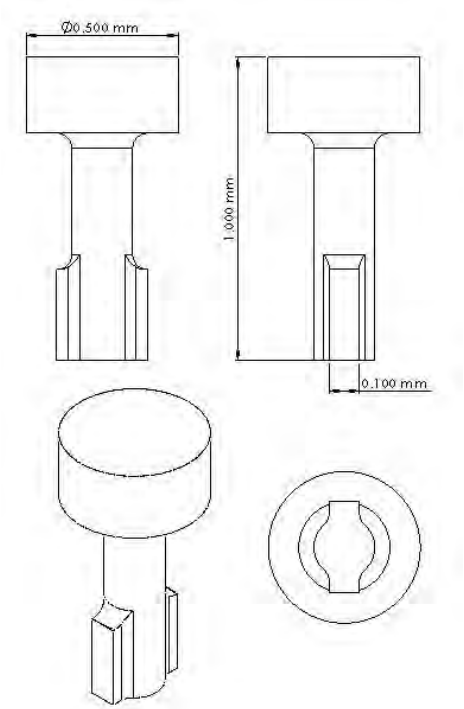

Figure 2.11: Mechanical drawing of anchor used to attach the larger magnet to the array.

This gave the tip of the implant a dipole moment of $9.25 \times 10^{-4}\ \mathrm{A} \cdot \mathrm{m}^2$. That is, a 67% increase in the magnet's diameter resulted in a 178% increase in the magnet's volume and strength.

The anchor was needed for the large magnet because of size constraints. The larger magnet would not fit inside the existing electrode-array mold with enough space for the silicone to encase the magnet. In order to attach the magnet, an anchor was fabricated using a Nano-Scribe 3D printer (Model Photonic Pro GT). The smaller end of the anchor was encased in silicone at the tip of the array, leaving the larger end of the anchor exposed to attach the magnet. Cyanoacrylate adhesive was used to attach the larger magnet to the anchor. The anchor caused the large-magnet array to be 1.8 mm longer that the small-magnet array, causing the most distal electrode to be farther from the tip of the array than in the small-magnet model. We believe that this problem could be circumvented with a minor redesign of the electrode array.

2.1.4 Magnetic Steering

Using the magnet embedded in the tip of the electrode array, the array can be steered as it is inserted into the scala tympani, using an externally generated magnetic field. If $\vec{b}$ (units T) is the magnetic field vector generated by the Omnimagnet at the location of the tip, and $\vec{m}$ (units A·m^2) is the dipole moment of the permanent magnet embedded in the tip, the torque (units N·m) applied to the tip of the implant is computed as

$$\vec{\tau} = \vec{m} \times \vec{b} \tag{2.1}$$

In order to generate the largest torque possible with a magnetic field of a given strength, the magnetic field is directed perpendicular to the dipole moment (i.e., the cylindrical axis of the permanent magnet).

Before insertion, paths are generated, corresponding to the position of the tip of the electrode array at each insertion depth. The path used for these experiments was created by Cohen et al. [3], with a small modification described by Clark et al. [2]. This path approximates the resting position of the array in our scala-tympani phantom. These path points are then associated with the desired magnetic field corresponding to each insertion depth.

The path is defined using parametric equations. θ is the angle of the cochlea, with $\theta = 0$ aligned with the $-y$ axis, and with θ increasing with positive rotation about the x axis (i.e., counter-clockwise in Figure 2.12). Only portions of the path in which magnetically steering is generated are defined below. The radius of curvature (R) of the path is

$$R = C(1 - D\ln(\theta_{\text{mod}} - \theta_0)) \quad : \quad 27.9^\circ \leq \theta < 100^\circ \tag{2.2}$$

$$R = Ae^{-B\theta_{\text{mod}}} \quad : \quad 100^\circ \leq \theta \leq 386^\circ \tag{2.3}$$

where

$$\theta_{\text{mod}} = 0.0002\theta^2 + 0.98\theta \tag{2.4}$$

and $A = 3.762\,\text{mm}$, $B = 0.001317\,\text{mm}$, $C = 7.967\,\text{mm}$, $D = 0.1287\,\text{mm}$, and $\theta_0 = 5^\circ$

The parametric equations defining the path's position are then

$$x = 0 \tag{2.5}$$

$$y = -R\cos(\theta) \tag{2.6}$$

$$z = -R\sin(\theta) \tag{2.7}$$

Taking analytical derivatives of each of the equations x, y and z with respect to θ, tangent vectors to the path can be calculated as

$$\vec{r} = \begin{bmatrix} \frac{dx}{d\theta} & \frac{dy}{d\theta} & \frac{dz}{d\theta} \end{bmatrix}^T \tag{2.8}$$

These are shown in blue in Figure 2.12(a).

Finally, the desired magnetic field vector $\vec{b}$ is calculated as

$$\vec{b} = -\|\vec{b}\|\vec{z} \quad : \quad 27.9^\circ \leq \theta < 100^\circ \tag{2.9}$$

$$\vec{b} = \|\vec{b}\| \left(\vec{x} \times \frac{\vec{r}}{||\vec{r}||} \right) \quad : \quad 100^\circ \leq \theta \leq 386^\circ \tag{2.10}$$

where the field's magnitude $\|\vec{b}\|$ is shown in Figure 2.13.

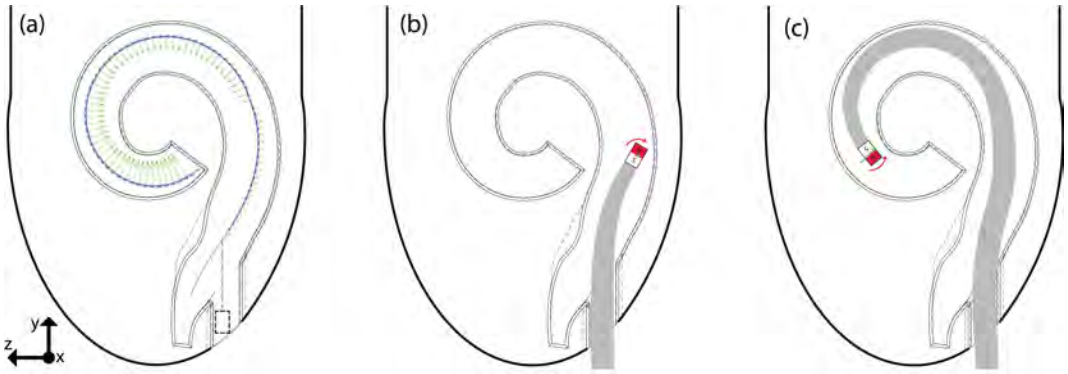

Figure 2.12: Magnetic steering of the electrode array. (a) Precomputed path as defined by parametric equations. The magnetic steering, indicated by green arrows, starts at 27.9°. Blue arrows define the vector tangent to the path. The dotted line defines the portion of path without any magnetic steering. (b) Array near the start of the channel, with the magnetic field shown with a green arrow and the magnetic torque depicted with a red arrow. (c) Array near the end of the channel.

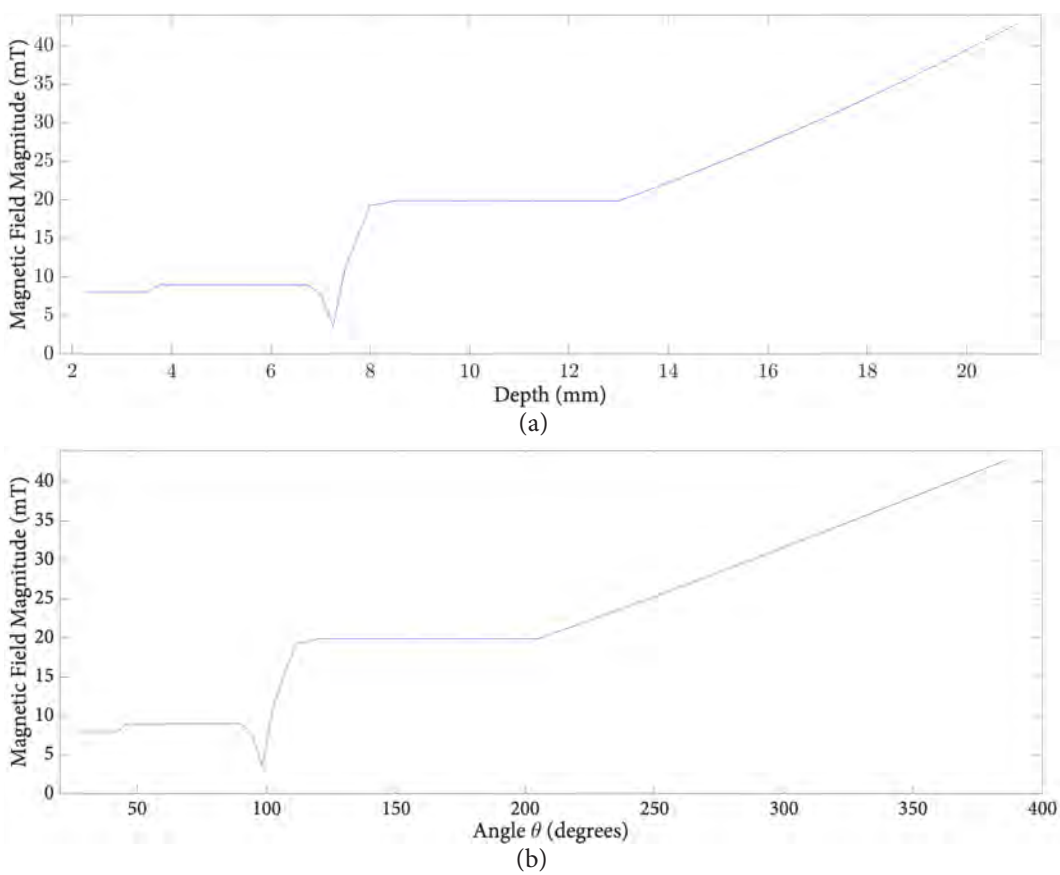

Figure 2.13: Magnitude of magnetic field, $\|\vec{b}\|$ versus (a) insertion depth, and (b) angle θ.

The trajectory for robotic insertion with magnetic steering was generated as follows. The path angle was integrated at high resolution (0.05°), starting from $\theta = 10.3°$, to determine waypoints corresponding to each 0.25 mm of electrode-array insertion, resulting in 85 total waypoints. Each of these waypoints was associated with respective magnetic field vectors, which were found during pilot testing. The magnetic field vectors at these waypoints are depicted in Figure 2.12(a). The complete trajectory was stored in a lookup table for use at run time; this lookup table is provided as Appendix B.

2.2 Experimental Design

We use a repeated-measures design to characterize force on the basilar membrane using one treatment variable and one blocking variable. The treatment variable (Array Type) has three levels: *Nonmagnetic*, *Small Magnet*, and *Large Magnet*. The blocking variable (Array Rotation), which is included to mitigate potential confounding factors related to plastic deformation of the electrode arrays after repeated insertion, has four levels of rotation about the array's central axis at the proximal end: 0°, 90°, 180°, and 270°. Insertion experiments were separated into three blocks, with each block comprising three sequential insertions at each of the four levels of Array Rotation—with order chosen at random, without replacement—for each of the three levels of Array Type, with *Large Magnet* being performed first due to its slightly longer length than the other two types, and then alternating between *Small Magnet* and *Nonmagnetic*. This resulted in 36 total insertions for each level of Array Type.

Under the conjecture that magnetic steering may do more harm than good if it is not being applied in the correct direction, we subsequently conducted four more experiments to characterize the effect of an error in our estimate of the modiolar axis (which is parallel to the x-axis in Figure 2.12). Each of these four experiments considered a rotational error of 10° in one of four directions: about the y-axis and about the z-axis, in each of the positive and negative directions. Each of these four experiments were designed similar to our principal experiment described above, but with three differences: only one level of Array Type was considered (*Large Magnet*), only three values of Array Rotation were considered (0°, 90°, and 180°), and only one block of data was collected. This resulted in three total insertions for each type of modiolar-axis error. The rationale for only considering

large-magnet arrays was based upon the results observed in the principal experiment. The rationale for performing fewer insertion trials was that our electrode arrays began to accumulate plastic deformation, and we did not need to collect more data to observe statistically significant results.

It should be noted that, although modiolar-axis estimation error is likely to be the main source of magnetic-steering error, other potential sources of error include error in the position estimate of the cochlea relative to the external magnetic-field source, calibration error of the external magnetic-field source, or misalignment of the permanent magnet attached to the tip of the electrode array. However, our choice of 10° modiolar-axis error was designed to be robust in order to approximate some of these other sources of error. In clinical practice, a CT scan of the patient can be used to estimate the modiolar axis [4, 21], and the most recent and most effective of these methods results in an average error of 2.5°[21].

2.3 Experimental Procedure

The phantom cochlea was covered with the thin plastic membrane, and the phantom cochlea was raised into and aligned with the force sensor. The force sensor was zeroed, and artificial perilymph was then pumped into the cochlea via the tube shown in Figure 2.6. The implant of choice was then loaded into the insertion device. The Omnimagnet was aligned first, followed by a coarse alignment of the insertion device using the articulating arm. Both alignments used the Polaris Spectra optical tracking system to ensure proper alignment. A fine alignment was then performed with the Newport three-degrees-of-freedom linear stage. This fine alignment was done using visual feedback from the digital microscope shown in Figure 2.8. The start point for the tip of each implant is shown by the dashed box shown in Figure 2.12(a).

Three blocks of data were collected during testing. Each block of data consisted of 12 insertions total for each array type (nonmagnetic, small magnet, and large magnet), for a total of 36 insertions for each array type ($n = 36$) in the study. Within each block, insertions with the large-magnet arrays were performed first, followed by small-magnet and nonmagnetic insertions. Small-magnet and nonmagnetic insertion sets took place consecutively, alternating which array type was done first, since the same implant was

used for these two types of insertion. The 12 insertions per array type were further divided into rotations about the central axis of the implant (0°, 90°, 180°, and 270°). These four rotations were chosen randomly without replacement. Implants were rotated to mitigate the effects of any plastic deformation that had occurred to the implant during previous insertions. Dividing the 12 insertions by four unique rotations resulted in three insertions per rotation; these three insertions were done consecutively and are defined as an insertion set.

Some of the insertions induced buckling of the portion of the array that was outside of the scala-tympani channel. If this occurred, the insertion would be stopped prematurely to ensure that no major plastic deformation of the array would occur and the array would be straightened out by hand.

All insertions were performed at a rate of 1.3 mm/s. Also, to reduce high-frequency noise in the force data, all data collected were postprocessed with a moving-average filter with a window size of 50 (i.e., 50 ms).

CHAPTER 3

RESULTS

The results for the principal experiment are shown in Figure 3.1, with results depicted as mean basilar-membrane forces with 95% confidence intervals, as a function of insertion depth (measured from the cochleostomy opening). Recall that the reported forces represent the integration of all basilar-membrane forces distributed along the length of the inserted electrode array at each given depth. We find that the large-magnet electrode array results in a statistically significant reduction in force compared to the nonmagnetic array for depths of approximately 14.4 mm and beyond. The difference in force becomes more pronounced with increasing insertion depth. We do not find a significant reduction in basilar-membrane force when using the small-magnet array, at any depth.

Going beyond the specific statistical experiment described above, considering our complete data set in its entirety is also informative. Figure 3.2 presents the data with bounds showing the minimum and maximum basilar-membrane forces observed, at each depth, across 36 insertions per array type. It is evident that the worst-case force observed with the large-magnet array is substantially smaller than the worse-case forces observed in either of the other two cases, including in the critical region from 180° to 270° where damage to the basilar membrane is most prevalent.

The results for the four experiments in which we consider 10° errors in the estimation of the modiolar axis are shown in Figure 3.3, with results depicted as mean basilar-membrane forces with 95% confidence intervals, as a function of insertion depth. Recall that we only consider the large-magnet array here, due to the poor performance of the small-magnet array in the previous experiment. Note that the confidence intervals here are quite wide due to the limited number of trials.

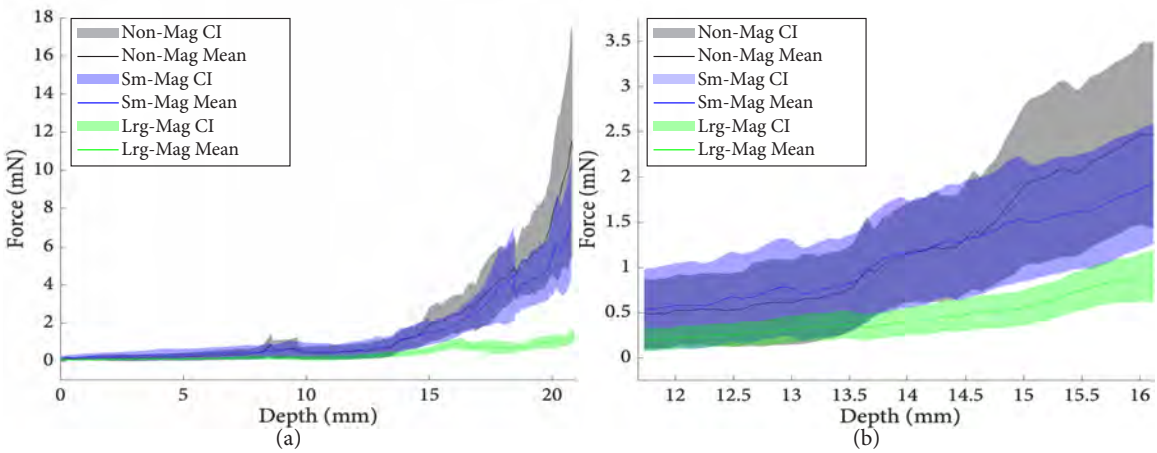

Figure 3.1: Force on the phantom basilar membrane as a function of insertion depth, shown as a mean and 95% confidence interval ($n = 36$). (a) Complete insertion. (b) Critical region from 180°to 270°.

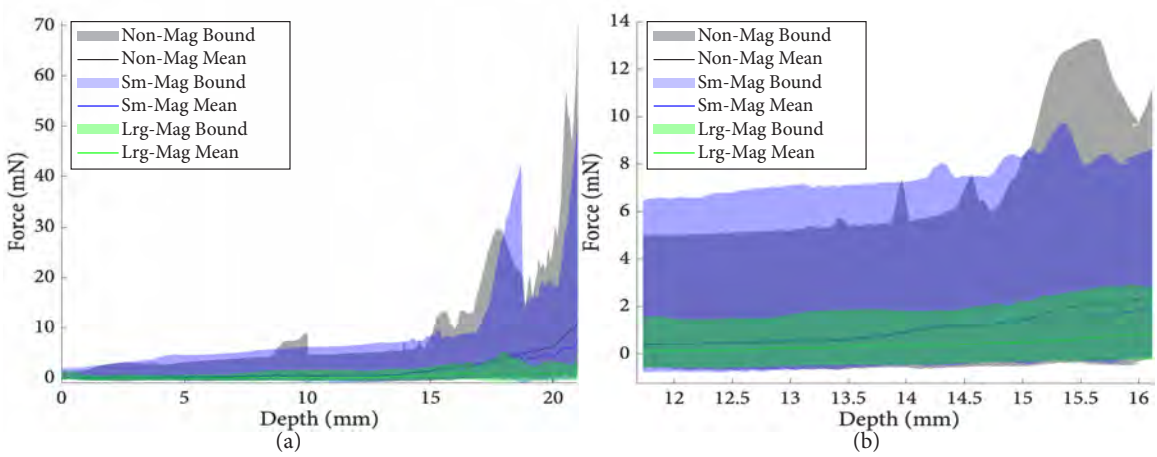

Figure 3.2: Force on the phantom basilar membrane as a function of insertion depth, shown as the minimum and maximum bounds of the complete data set ($n = 36$). (a) Complete insertion. (b) Critical region from 180°to 270°.

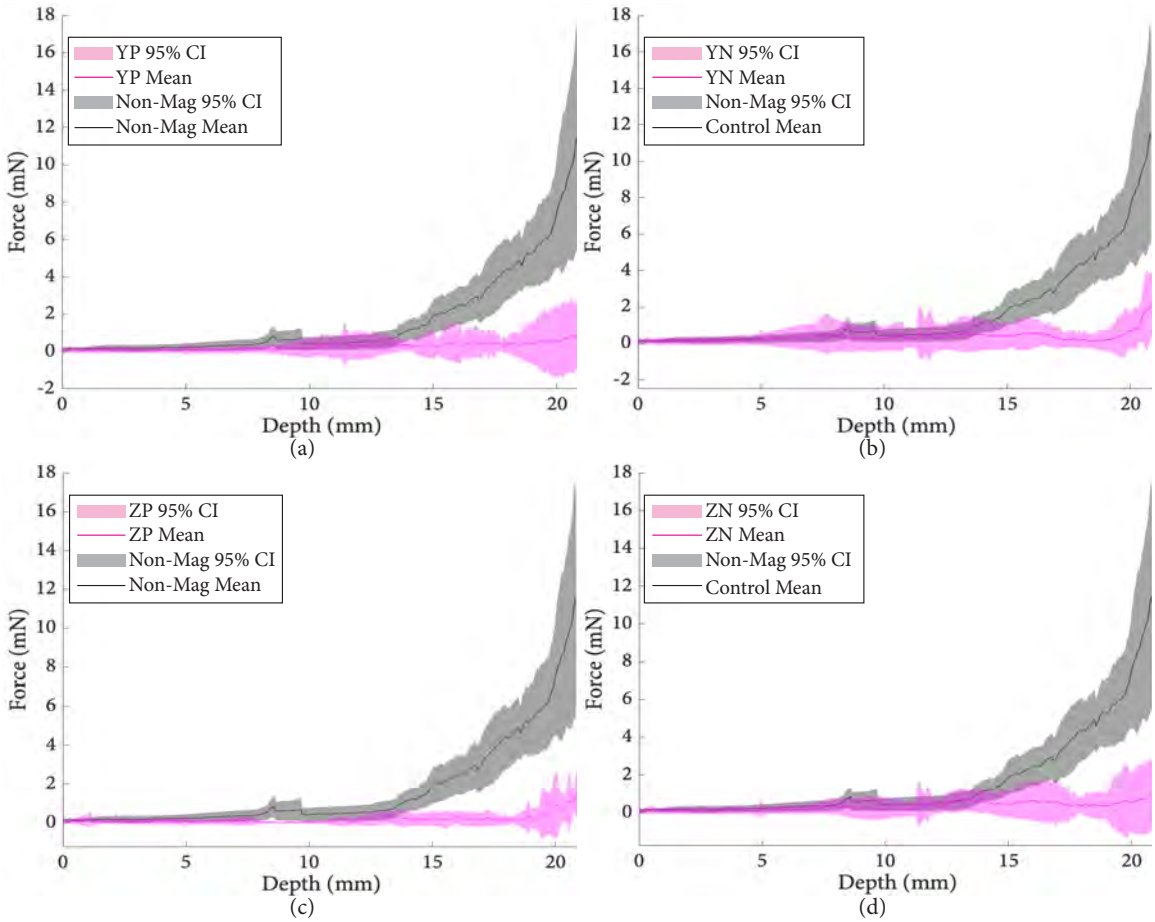

Figure 3.3: Force on the phantom basilar membrane as a function of insertion depth, shown as a mean and 95% confidence interval ($n = 3$). Each plot compares insertions with error in magnetic steering to the nonmagnetic case. (a) Error about the positive y-axis. (b) Error about the negative y-axis. (c) Error about the positive z-axis. (d) Error about the negative z-axis.

However, even accounting for this, we still find a statistically significant reduction in force for depths of approximately 17 mm (conservatively) and beyond.

Figure 3.4 presents the same data with bounds showing the minimum and maximum basilar-membrane forces observed, at each depth, across three insertions per array type. There is a stark contrast between the two array types, with the worst-case force observed with the large-magnet array being substantially smaller than the worse-case forces observed without magnetic steering. Our limited data make this observation somewhat anecdotal, but it does provide evidence that magnetic steering is providing substantial benefits, even with nonnegligible error in the magnetic steering.

It is also interesting to compare the results for insertions with error in the estimation

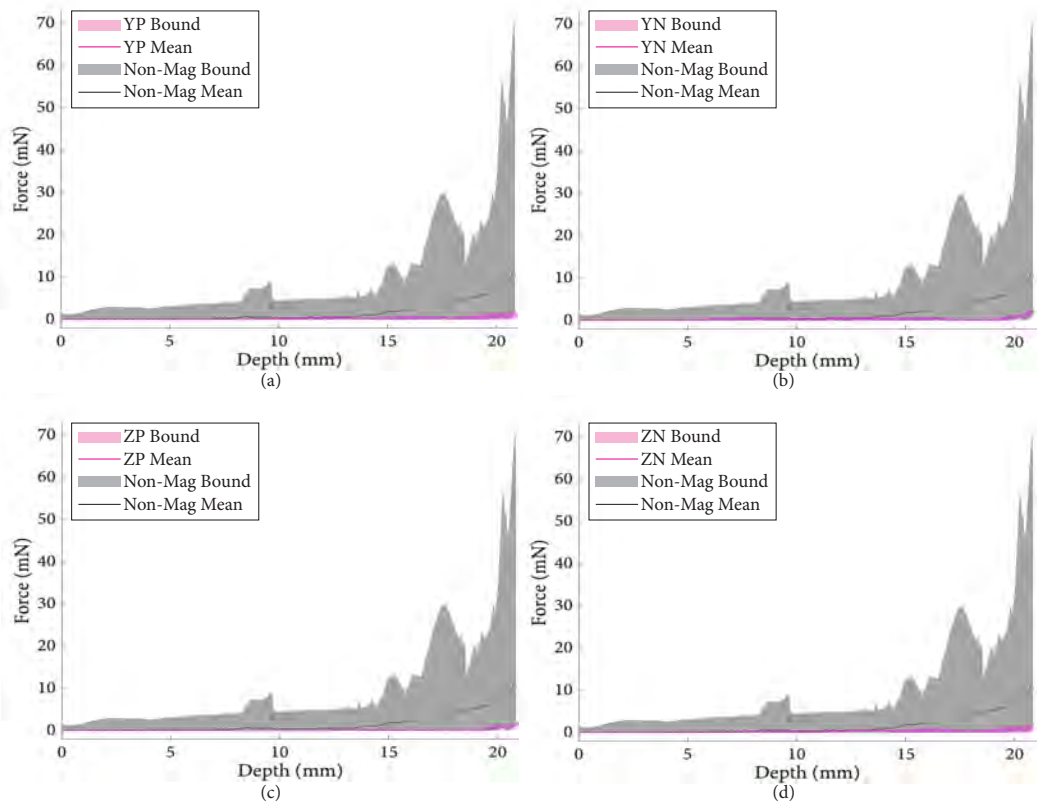

Figure 3.4: Force on the phantom basilar membrane as a function of insertion depth, shown as minimum and maximum bounds of the complete data set ($n = 3$). Each plot compares insertions with error in magnetic steering to the nonmagnetic case. (a) Error about the positive y-axis. (b) Error about the negative y-axis. (c) Error about the positive z-axis. (d) Error about the negative z-axis.

of the modiolar axis to the results for magnetically steered insertions with an accurate model of the modiolar axis. We do not find a statistically significant difference (Figure 3.5). However, we do find some evidence suggesting that error in magnetic steering does result in a small increase in basilar-membrane forces (Figure 3.6).

Figure 3.7 summarizes the statistically significant improvement that magnetic steering provides relative to insertions without magnetic steering, for all of the cases considered in this study. The depth at which a significant difference is first observed is different in each of the five cases tested, but all cases are significantly different beyond a depth of approximately 17 mm. We see that the force on the basilar membrane is in the range of 3–38% of what it would be at the equivalent depth without magnetic steering.

Figure 3.8 shows example insertions without the force plate in place, so that deformation of the membrane can be visualized, demonstrating the force that the electrode array

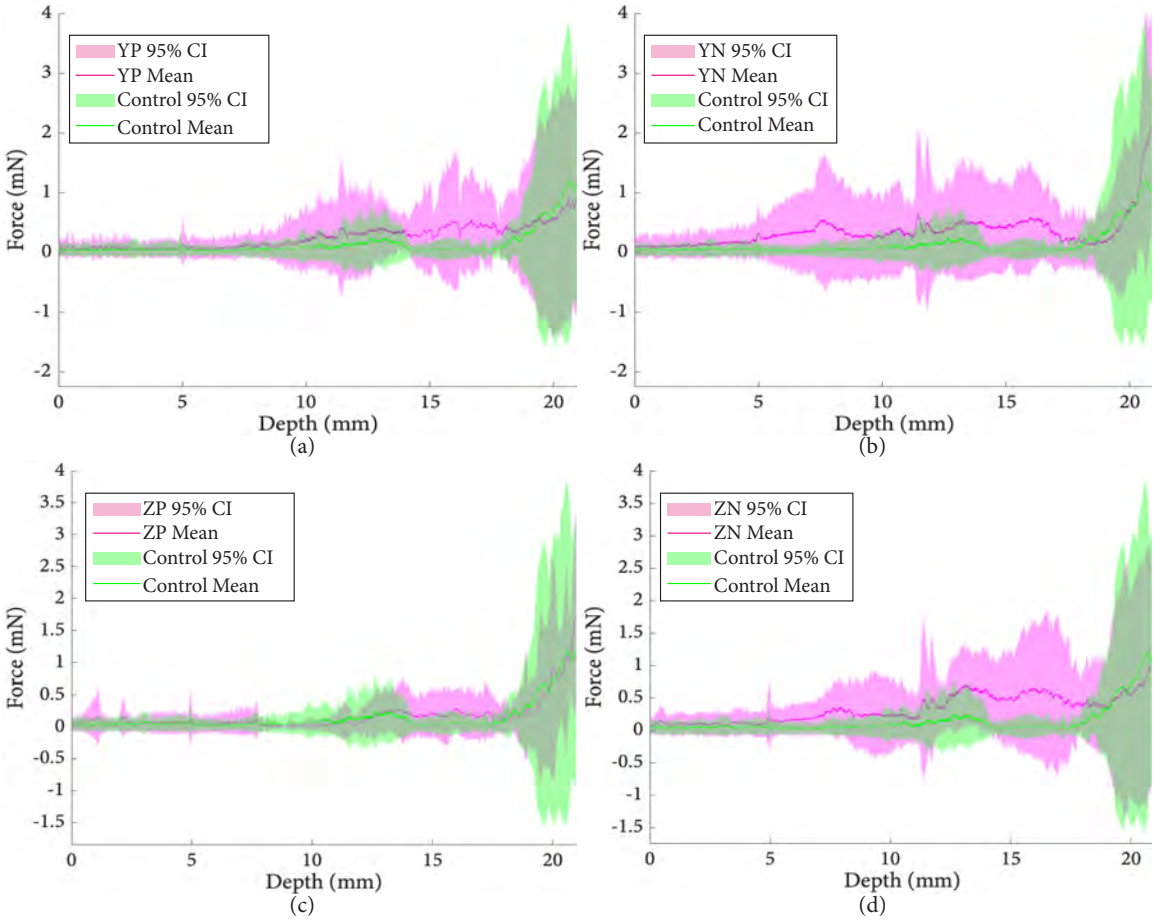

Figure 3.5: Force on the phantom basilar membrane as a function of insertion depth, shown as a mean and 95% confidence interval ($n = 3$). Each plot compares insertions with error in magnetic steering to the control case without error in magnetic steering. (a) Error about the positive y-axis. (b) Error about the negative y-axis. (c) Error about the positive z-axis. (d) Error about the negative z-axis.

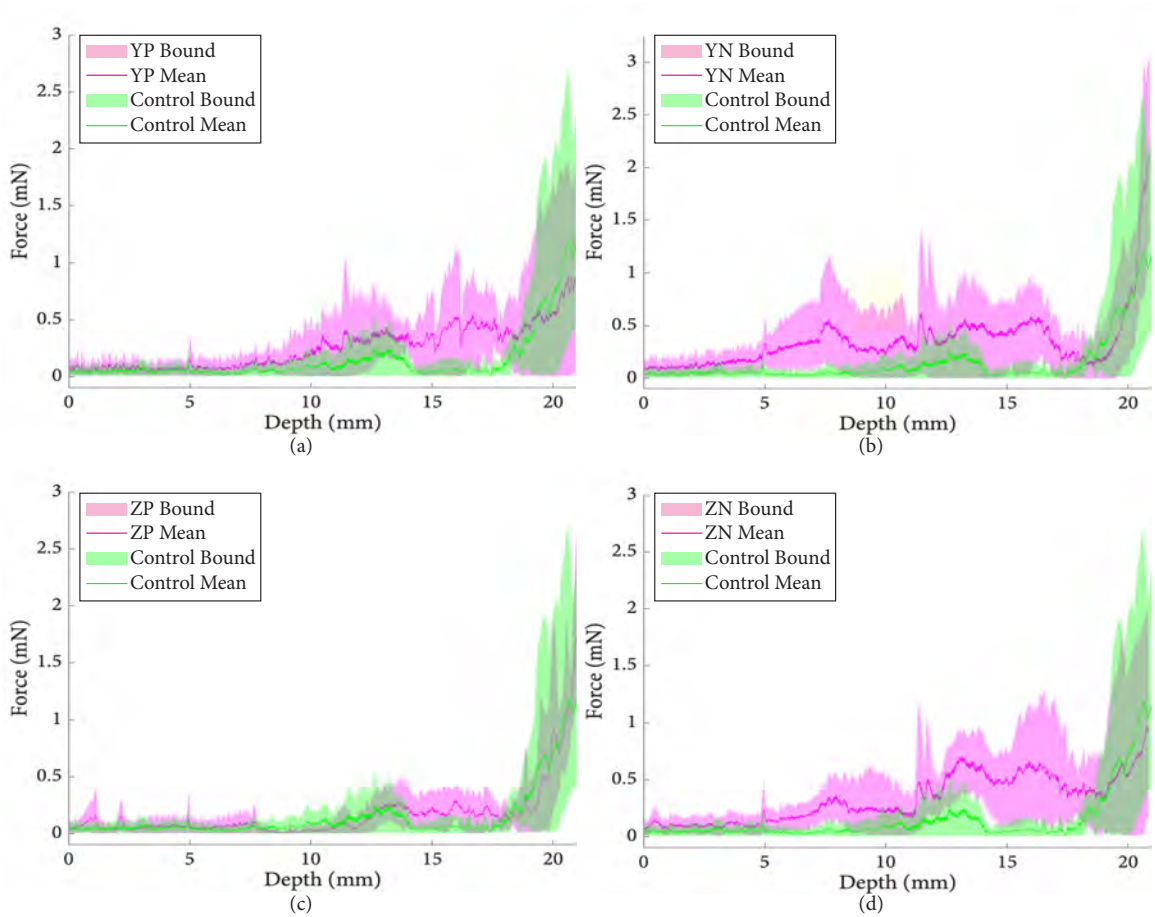

Figure 3.6: Force on the phantom basilar membrane as a function of insertion depth, shown as minimum and maximum bounds of the complete data set ($n = 3$). Each plot compares insertions with error in magnetic steering to the control case without error in magnetic steering. (a) Error about the positive y-axis. (b) Error about the negative y-axis. (c) Error about the positive z-axis. (d) Error about the negative z-axis.

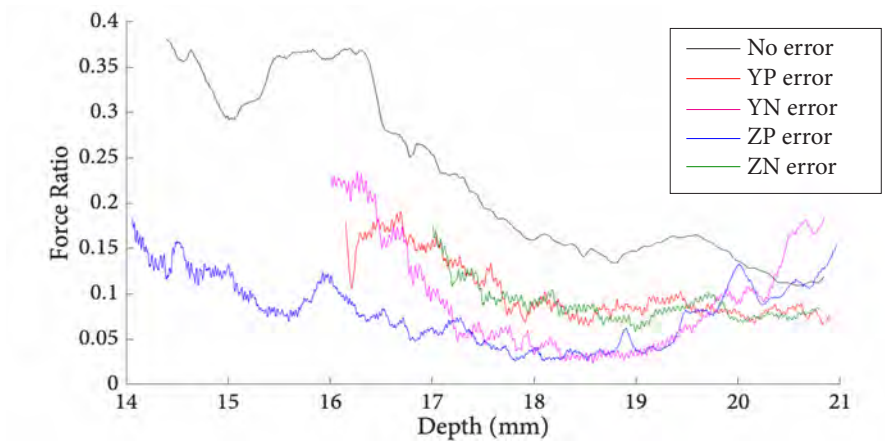

Figure 3.7: Ratio of the mean basilar-membrane force with the large-magnet array to the mean basilar-membrane force with the nonmagnetic array, for each of the five cases tested.

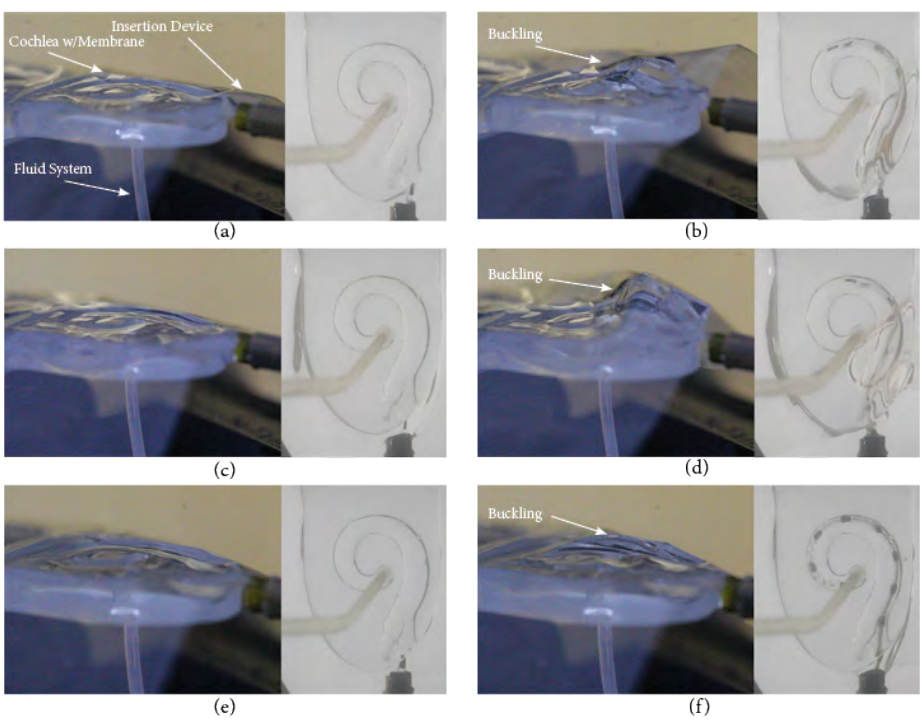

Figure 3.8: Visualizing insertions without the force plate in place. Deformation of the membrane demonstrates the force that the electrode array puts on the membrane. Images include: nonmagnetic array (a) initial condition and (b) at depth = 15.16 mm; small-magnet array (c) initial condition and (d) at depth = 14.87 mm; and large-magnet array (e) initial condition and (f) at depth = 21.00 mm.

puts on the membrane. In the results for the nonmagnetic array, the array can be seen to deviate significantly out of the channel; this began at approximately 90°and continued to 250°for this specific run. The results for the small-magnet array are qualitatively similar. The results for the large-magnet array are qualitatively superior to the other two; deviations out of the channel began at approximately 90°and continued to 270°, but it is evident that the force on the membrane never reached the same level as the other two.

CHAPTER 4

DISCUSSION

The results for our principal experiment, depicted in Figure 3.1, indicated that there was not a significant reduction in basilar-membrane force when using the small-magnet electrode array, compared to nonmagnetic insertions, at any depth. This result is not trivial, considering that we would expect to see a reduction in insertion force for this case [10]. With the small-magnet array, a portion of the torque required to bend the array, which is naturally straight, is being provided by the magnetic steering. As a result, the forces being applied by the walls of the scala tympani are necessarily less; this is the cause of the reduction in insertion force. However, with the small-magnet array, we did not observe the tip of array leave the walls of the scala tympani, whereas we did observe the tip of the large-magnet array leave the walls of the scala tympani. This suggests that, although any amount of magnetic steering will provide some reduction in insertion force, for the protection of the basilar membrane it is important to generate enough magnetic torque to cause the tip of the array to move away from the walls of the scala tympani (at least in the critical region in which damage to the basilar membrane is most likely to occur).

The magnetic-steering system used has a current limit of 30 A. Current can briefly be increased up to 50 A, but the AMC current amplifiers will engage the current limit to drop the current back to 30 A. During all magnetic insertions, the system was configured to use as much of the maximum 30 A as possible along with short bursts above 30 A. Because magnetic torque is the product of the strength of the magnet field and the strength of the embedded permanent magnet, it is possible to get the same results from this study with the smaller embedded magnet as long as the magnetic torque is unchanged. This would either involve an Omnimagnet that can source more current (and dissipate the associated heat) more effectively by adding cooling, a larger Omnimagnet, or a permanent magnet as the external source.

CHAPTER 5

CONCLUSION

In this thesis, forces on the basilar membrane were measured in-vitro using a custom instrumented scala-tympani phantom. Forces imparted on the phantom basilar membrane were compared between robotic insertions with and without magnetic steering. We demonstrated that magnetic steering, of sufficient magnitude, significantly reduces forces on the basilar membrane for insertion depths beyond 14.4 mm, which includes the critical region in which damage to the basilar membrane most commonly occurs. This study provides the first compelling evidence that magnetic steering of robotically inserted electrode arrays will provide protection to the basilar membrane, compared to robotic insertion without magnetic steering.

APPENDIX A

CALIBRATING THE OMNIMAGNET

The Omnimagnet was designed such that its field could be accurately modeled using the dipole-field model, but that simple model loses accuracy at locations that are inside 150% of the Omnimagnet's minimum bounding sphere [15]. Since we are conducting experiments in this reduced-accuracy region, we chose to not make the dipole-field assumption, and instead create a calibrated model that describes the magnetic field at a given position (i.e., the nominal position at which we would place the center of the scala-tympani phantom). This calibration was performed by activating each coil individually, starting with 1 A and increasing in 1 A increments until 14 A was reached. The magnetic field was measured at the point of interest and divided by the input current. An average of all these readings was used to generate the actuation matrix. It is known that the effect of the three currents affect the resulting field linearly, so this average can be scaled and superimposed. These three magnetic-field vectors can be recorded in the columns of an actuation matrix A:

$$A = \begin{bmatrix} \vec{b}_{o,x} & \vec{b}_{m,x} & \vec{b}_{i,x} \\ \vec{b}_{o,y} & \vec{b}_{m,y} & \vec{b}_{i,y} \\ \vec{b}_{o,z} & \vec{b}_{m,z} & \vec{b}_{i,z} \end{bmatrix} \tag{A.1}$$

where $\vec{b}_o$, $\vec{b}_m$, and $\vec{b}_i$ are the magnetic fields generated by the outer, middle, and inner Omnimagnet coils, respectively. The actuation matrix maps the 3×1 array of input currents I to the resulting field $\vec{b}$ at a location of interest:

$$\vec{b} = AI \tag{A.2}$$

The necessary currents to achieve some desired field $\vec{b}_{\text{des}}$ are then are calculated as

$$I = A^{-1}\vec{b}_{\text{des}} \tag{A.3}$$

At the location used in this study, the calibrated actuation matrix (in units mT) is

$$A = \begin{bmatrix} -1.69711 & -0.536467 & 0.368865 \\ -0.426764 & 1.18526 & 0.0789854 \\ 0.23188 & 0.0626704 & 1.21083 \end{bmatrix} \tag{A.4}$$

APPENDIX B

TRAJECTORY FOR ROBOTIC INSERTION WITH MAGNETIC STEERING

Waypoint	x Field mT	y Field mT	z Field mT	Insertion Depth mm	Angle θ °
1	0	0	0	0	10.30
2	0	0	0	0.26	11.57
3	0	0	0	0.51	12.98
4	0	0	0	0.75	14.58
5	0	0	0	1.00	16.38
6	0	0	0	1.25	18.38
7	0	0	0	1.50	20.52
8	0	0	0	1.75	22.86
9	0	0	0	2.00	25.29
10	0	0	−8	2.25	27.92
11	0	0	−8	2.50	30.60
12	0	0	−8	2.75	33.42
13	0	0	−8	3.00	36.34
14	0	0	−8	3.25	39.36
15	0	0	−8	3.50	42.48
16	0	0	−9	3.75	45.69
17	0	0	−9	4.00	48.95
18	0	0	−9	4.25	52.36
19	0	0	−9	4.50	55.76
20	0	0	−9	4.75	59.32
21	0	0	−9	5.00	62.92
22	0	0	−9	5.25	66.57
23	0	0	−9	5.50	70.32
24	0	0	−9	5.75	74.11
25	0	0	−9	6.00	78.01
26	0	0	−9	6.25	81.95
27	0	0	−9	6.50	85.94
28	0	0	−9	6.75	90.03
29	0	0	−7.73	7	94.17
30	0	0	3.65	7.25	98.40
31	0	−2.61	10.99	7.50	102.69
32	0	−5.63	14.33	7.75	107.02

33	0	−8.18	17.49	8.00	111.40
34	0	−10.09	16.71	8.25	115.83
35	0	−12.08	15.81	8.50	120.26
36	0	−13.28	14.82	8.75	124.69
37	0	−14.40	13.73	9.00	129.17
38	0	−15.44	12.55	9.25	133.69
39	0	−16.39	11.28	9.50	138.22
40	0	−17.24	9.93	9.75	142.79
41	0	−17.98	8.51	10	147.42
42	0	−18.61	7.02	10.25	152.04
43	0	−19.12	5.48	10.50	156.67
44	0	−19.51	3.89	10.75	161.34
45	0	−19.76	2.26	11	166.06
46	0	−19.88	0.61	11.25	170.83
47	0	−19.86	−1.06	11.50	175.60
48	0	−19.70	−2.73	11.75	180.42
49	0	−19.39	−4.39	12.00	185.24
50	0	−18.95	−6.03	12.25	190.11
51	0	−18.36	−7.63	12.50	195.02
52	0	−17.63	−9.19	12.75	199.94
53	0	−16.75	−10.69	13	204.95
54	0	−16.21	−12.48	13.25	209.92
55	0	−15.48	−14.27	13.50	214.98
56	0	−14.56	−16.04	13.75	220.04
57	0	−13.43	−17.77	14.00	225.15
58	0	−12.10	−19.44	14.25	230.31
59	0	−10.56	−21.02	14.50	235.52
60	0	−8.82	−22.49	14.75	240.73
61	0	−6.88	−23.83	15.00	245.99
62	0	−4.76	−25.01	15.25	251.29
63	0	−2.46	−26.01	15.50	256.65
64	0	0.01	−26.79	15.75	262.05
65	0	2.63	−27.35	16	267.45
66	0	5.38	−27.64	16.25	272.95
67	0	8.23	−27.66	16.50	278.45
68	0	11.15	−27.38	16.75	284
69	0	14.11	−26.78	17.00	289.60
70	0	17.09	−25.86	17.25	295.25
71	0	20.05	−24.58	17.50	300.94
72	0	22.94	−22.96	17.75	306.69
73	0	25.73	−20.99	18.00	312.48
74	0	28.38	−18.65	18.25	318.32
75	0	30.83	−15.97	18.50	324.21
76	0	33.04	−12.95	18.75	330.15
77	0	34.97	−9.61	19.00	336.13
78	0	36.57	−5.98	19.25	342.17
79	0	37.79	−2.08	19.50	348.25
80	0	38.60	2.06	19.75	354.44

81	0	38.95	6.37	20	360.62
82	0	38.80	10.83	20.25	366.90
83	0	38.12	15.39	20.50	373.22
84	0	36.89	19.96	20.75	379.60
85	0	35.09	24.49	21.00	386.03

REFERENCES

[1] T. L. Bruns, K. E. Riojas, D. S. Ropella, M. S. Cavilla, A. J. Petruska, M. H. Freeman, R. F. Labadie, J. J. Abbott, and R. J. Webster III, *Magnetically steered robotic insertion of cochlear-implant electrode arrays: System integration and first-in-cadaver results*, IEEE Robot Autom Lett, 5 (2020), pp. 2240–2247.

[2] J. R. Clark, F. M. Warren, and J. J. Abbott, *A scalable model for human scala-tympani phantoms*, J Med Devices, 5 (2011), p. 014501.

[3] L. T. Cohen, J. Xiu, S. A. Xu, and G. M. Clark, *Improved and simplified methods for specifying positions of the electrode bands of a cochlear implant array*, Am J Otolaryng, 17 (1996), p. 859–865.

[4] T. Demarcy, C. Vandersteen, N. Guevara, C. Raffaelli, D. Gnansia, N. Ayache, and H. Delingette, *Automated analysis of human cochlea shape variability from segmented µct images*, Comput Med Imag Grap, 59 (2017), pp. 1–12.

[5] A. Dhanasingh and C. Jolly, *An overview of cochlear implant electrode array designs*, Hearing Res, 356 (2017), pp. 93–103.

[6] H. Gray, *Gray's Anatomy*, Running Press, 1974.

[7] D. R. Ketten, M. W. Skinner, G. Wang, M. W. Vannier, G. A. Gates, and J. Gail Neely, *In vivo measures of cochlear length and insertion depth of nucleus cochlear implant electrode arrays*, Ann Otol Rhinol Laryngol, 107 (1998), pp. 1–16.

[8] H. Kha and B. Chen, *Finite element analysis of damage by cochlear implant electrode array's proximal section to the basilar membrane*, Otol Neurotol, 33 (2012), pp. 1176–1180.

[9] L. Leon, M. S. Cavilla, M. B. Doran, F. M. Warren, and J. J. Abbott, *Scala-tympani phantom with cochleostomy and round-window openings for cochlear-implant insertion experiments*, J Med Devices, 8 (2014), p. 041010.

[10] L. Leon, F. M. Warren, and J. J. Abbott, *An in-vitro insertion-force study of magnetically guided lateral-wall cochlear-implant electrode arrays*, Otol Neurotol, 39 (2018), pp. e63–e73.

[11] ——, *Optimizing the magnetic dipole-field source for magnetically guided cochlear-implant electrode-array insertions*, J Med Robot Res, 3 (2018), p. 1850004.

[12] O. Majdani, D. Schurzig, A. Hussong, T. Rau, J. Wittkopf, T. Lenarz, and R. F. Labadie, *Force measurement of insertion of cochlear implant electrode arrays in vitro: comparison of surgeon to automated insertion tool*, Acta Oto-Laryngol, 130 (2010), pp. 31–36.

[13] MED-EL, *How hearing works*. www.medel.com/en-us/about-hearing/how-hearing-works.

[14] W. Olsen, *Mayo Clinic on Hearing*, Mayo Clinic Health Information, 2003.

[15] A. J. Petruska and J. J. Abbott, *Omnimagnet: An omnidirectional electromagnet for controlled dipole-field generation*, IEEE T Magn, 50 (2014), p. 8400810.

[16] F. Risi, *Considerations and rationale for cochlear implant electrode design-past, present and future*, J Int Adv Otol, 14 (2018), pp. 382–391.

[17] D. Schurzig, R. J. Webster III, M. S. Dietrich, and R. F. Labadie, *Force of cochlear implant electrode insertion performed by a robotic insertion tool: comparison of traditional versus advance off-stylet techniques*, Otol Neurotol, 31 (2010), pp. 1207–1210.

[18] D. Schuster, L. B. Kratchman, and R. F. Labadie, *Characterization of intracochlear rupture forces in fresh human cadaveric cochleae*, Otol Neurotol, 36 (2015), pp. 657–661.

[19] G. B. Wanna, J. H. Noble, R. H. Gifford, M. S. Dietrich, A. D. Sweeney, D. Zhang, B. M. Dawant, A. Rivas, and R. F. Labadie, *Impact of intrascalar electrode location, electrode type, and angular insertion depth on residual hearing in cochlear implant patients: preliminary results*, Otol Neurotol, 36 (2015), pp. 1343–1348.

[20] P. Wardrop, D. Whinney, S. J. Rebscher, J. T. Roland Jr, W. Luxford, and P. A. Leake, *A temporal bone study of insertion trauma and intracochlear position of cochlear implant electrodes. I: Comparison of Nucleus banded and Nucleus Contour^{TM} electrodes*, Hearing Res., 203 (2005), pp. 54–67.

[21] W. Wimmer, C. Vandersteen, N. Guevara, M. Caversaccio, and H. Delingette, *Robust cochlear modiolar axis detection in ct*, in International Conference on Medical Image Computing and Computer-Assisted Intervention, Springer, 2019, pp. 3–10.

[22] J. Zhang, S. Bhattacharyya, and N. Simaan, *Model and parameter identification of friction during robotic insertion of cochlear-implant electrode arrays*, in 2009 IEEE International Conference on Robotics and Automation, IEEE, 2009, pp. 3859–3864.

[23] J. Zhang, W. Wei, J. Ding, J. T. Roland Jr, S. Manolidis, and N. Simaan, *Inroads toward robot-assisted cochlear implant surgery using steerable electrode arrays*, Otol Neurotol, 31 (2010), pp. 1199–1206.

[24] J. Zhang, K. Xu, N. Simaan, and S. Manolidis, *A pilot study of robot-assisted cochlear implant surgery using steerable electrode arrays*, in International Conference on Medical Image Computing and Computer-Assisted Intervention, Springer, 2006, pp. 33–40.